

Bearing Fault Diagnosis Based on Graph Formulation and Graph Convolutional Network

Xin Wang,¹ Wenjin Zhou,¹ and Xiaodong Li²

¹Research and Development Center of Smart Information and Communications Technologies, Shanghai Advanced Research Institute, Chinese Academy of Sciences, No.99 Haik Road, Shanghai 201210, China

²Key Laboratory of Noise and Vibration Research, Institute of Acoustics, Chinese Academy of Sciences, No. 21 North 4th Ring Road, Haidian District, Beijing 100190, China

(Received 22 October 2023; Revised 19 November 2023; Accepted 08 December 2023; Published online 08 December 2023)

Abstract: Bearing fault diagnosis stands as a critical component in the maintenance of rotating machinery. Many prevalent deep learning techniques are tailored to Euclidean datasets such as audio, image, and video. However, these methods falter when confronting non-Euclidean datasets, notably graph representations. In response, here we introduce an innovative approach harnessing the graph convolutional network (GCN) to analyze graph data derived from vibration signals related to bearing faults. This enhances the precision and reliability of fault diagnosis. Our methodology initiates by deriving a periodogram from the unprocessed vibration signals. Subsequently, this periodogram is mapped into a graph format, upon which the GCN is engaged for classification purposes. We substantiate the efficacy of our approach through rigorous experimental assessments conducted on a collection of ten bearing sets. Within these experiments, an accelerometer chronicles vibration signals across varying load conditions. We probe into the diagnostic accuracy rates across diverse loads and signal-to-noise ratios. Furthermore, a comparative evaluation of our method against several established algorithms delineated in this study is undertaken. Empirical observations confirm that our GCN-based strategy registers an elevated diagnostic accuracy quotient.

Keywords: bearing fault diagnosis; deep learning; graph convolutional network

I. Introduction

Bearings serve as foundational elements in rotating machinery, yet they remain among the most susceptible to wear and damage [1]. Faults in these bearings can critically jeopardize machine operator's safety and hinder industrial productivity. This underscores the crucial importance of bearing fault diagnosis within the overarching scope of rotating machinery maintenance—a topic that has garnered significant research interest over the past years [2].

At the heart of bearing diagnostic algorithms lie two principal components: the extraction of signal features and subsequent pattern classification. Various techniques facilitate signal feature extraction, including the fast Fourier transform (FFT) [3], wavelet analyses [4], empirical mode decomposition [5], and in-depth statistical signal evaluations [6], among others. On the pattern differentiation front, an array of algorithms has been devised, with notable mentions being support vector machines [7], back-propagation neural networks [8], Bayesian analytical tools [9], and proximity-based classifiers [10].

Deep learning, a burgeoning subset of machine learning, has exhibited exceptional capabilities, often surpassing human benchmarks, as evidenced by recent studies [11–13]. Its integration into fault diagnosis has become progressively pronounced. Diverging from conventional fault diagnosis techniques, deep learning delves into multi-layered networks, facilitating the incremental extraction of

input sample features. By leveraging nonlinear activation functions at every layer, it accomplishes autonomous feature extraction and classification. Consequently, this diminishes the reliance on manual feature extraction, substantially reducing the need for expert intervention and specialized know-how.

The graph convolutional network (GCN) emerges as an advanced deep learning methodology specifically tailored to handle non-Euclidean datasets, characterized by their unique nodes and interconnecting edges. Within GCNs, the convolutional operations on graphs adeptly extract pivotal features, harmoniously fusing local node attributes with overarching graph architecture. This prowess has already been evidenced in diverse domains, including image and text identification [14], objective classification [15], and motion detection [16].

The nascent intersection of graph theory with fault diagnosis has only begun to unfold in recent scholarly pursuits. For instance, the study in [17] adeptly converted time-sequence signals linked with bearing faults into graph structures, aiming to surveil the dynamic shifts in rotating machinery. Similarly, [18] encapsulated the time-frequency continuum of a bearing fault signal within a graph framework, employing the K Nearest Neighbor for subsequent classification. The research presented in [19] opted for an undirected weighted graph to encapsulate the frequency spectrum of a pertinent bearing fault signal. In [20], an intelligent acoustic-based fault diagnosis algorithm is proposed using deep graph neural network, the data collected by microphones are transformed into graphs, and a deep graph neural network is used to classify the fault bearings.

Corresponding author: Xiaodong Li (e-mail: lxid@mail.ioa.ac.cn).

In [21], time-domain signal segments of bearing are used as the node features of a graph, and a graph convolutional neural network is proposed to process the transformed graph to make a classification. Nonetheless, these pioneering endeavors remain in their embryonic phases, and their diagnostic precision has room for enhancement.

Drawing inspiration from prior research and advancements in the realm of fault diagnosis, this paper introduces a novel deep learning approach rooted in GCN aimed at enhancing the precision and resilience of bearing fault diagnosis. Within this framework, vibration signals are concurrently amassed via an accelerometer and subsequently transmuted into a periodogram. We then develop a graph formulation technique to represent this periodogram. Conclusively, an innovative GCN architecture is posited to manage these graph representations. Experimental validations ensue, juxtaposing the results garnered from our approach against prevailing algorithms. Our findings underscore the superior diagnostic precision our methodology offers.

This study's pivotal contributions can be distilled into two main aspects: (1) The introduction of a novel GCN configuration and (2) a fresh approach to encapsulating bearing fault vibration signals within a graph-centric paradigm.

The structure of this paper unfolds as follows: Section II delves into the principles underpinning GCN. Section III elucidates our novel technique of transfiguring vibration signals into graph representations, in tandem with a detailed exposition of our bespoke GCN algorithm. Section IV embarks on an analytical journey through bearing fault signals, showcasing results obtained via our method, and subsequently benchmarking our method's performance against established algorithms across varied loads and signal-to-noise ratios (SNRs). Section V culminates with our conclusive remarks.

II. GCN

A standard GCN is comprised of several layers: the input, graph convolutional, graph-pooling, fully connected, and output layers.

In the GCN's input layer, non-Euclidean graphs are adeptly processed. Such graphs encapsulate the inherent geometry and structural nuances of data, often delivering richer insights than traditional data configurations.

Delving into the graph convolutional layer, the convolutional kernel conducts convolutions on the data received from the preceding layer. Coupled with a nonlinear activation function, this layer crafts the resultant output features. The product of each layer embodies the convolutional synthesis of myriad input attributes. Its mathematical framework is delineated in reference [22]:

$$H^{(l+1)} = f(\widehat{D}^{-1/2} \widehat{A} \widehat{D}^{-1/2} H^{(l)} W^{(l)}) \quad (1)$$

where $\widehat{A} = A + I$, in which A is the adjacency matrix, I signifies the identity matrix, and \widehat{D} represents the diagonal node degree matrix of \widehat{A} ; the factor $\widehat{D}^{-1/2} \widehat{A} \widehat{D}^{-1/2}$ normalizes nodes possessing a significant degree and is referred to as the normalized adjacency matrix; $H^{(l)}$ is the feature matrix at the layer l , whereas $W^{(l)}$ stands for the weight matrix at the same layer.

In order to further investigate the characteristics of the graph convolutional operation, an analogy is made between

the 2D convolution operation and graph convolutional operation. Figure 1(a) represents the 2D convolutional operation on image data, and Fig. 1(b) represents the graph convolutional operation. An image can be considered as a special case of the graph in which pixels are connected by adjacent pixels. Analogously, the image pixels and their spatial relationships correspond to graph nodes and graph edges, respectively, and 2D convolutional kernels are extended to graph convolutional kernels so as to compute the sum-of-product over neighboring nodes.

Subsequent to graph convolutional operations, an activation function introduces a nonlinear transformation to the logits-value output for each convolution. This function's role is pivotal in transposing inherently linearly non-separable multidimensional features into a space where their linear separability is augmented. This study employs the ReLU function as the chosen activation function, a choice driven by its beneficial property: its derivative remains constant at 1 for any input exceeding 0, effectively addressing the gradient dispersion concern. The ReLU function is represented as:

$$f(x) = \max\{0, x\} \quad (2)$$

To enhance the GCN's efficiency by curbing its parameter count, the graph-pooling layer streamlines a substantial graph into a more compact version through down-sampling, thereby mitigating computational demand in subsequent stages.

The fully connected layer extends the preceding layer's output into a unidimensional vector, serving as the input of this layer. The layer then facilitates a comprehensive linkage between the input and output, assimilating the diversified local data from earlier graph convolutional or graph-pooling layers.

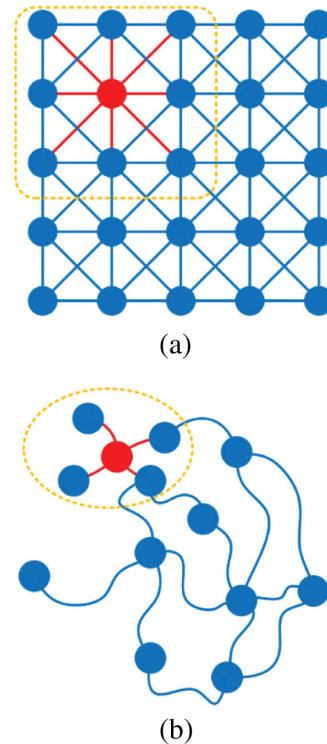


Fig. 1. 2D convolution vs. graph convolution: (a) 2D convolution, (b) graph convolution.

Typically, the output layer employs the softmax classifier to generate classification labels. Recognized as a prevalent linear classifier, the softmax classifier emerges as a variant of multi-class classification, rooted in logistic regression. Here,

$$\text{softmax}(z^o(j)) = \frac{e^{z^o(j)}}{\sum_{k=1}^M e^{z^o(k)}} \quad (3)$$

where $z^o(j)$ designates the logits emanating from the j^{th} neuron at the output layer, while M denotes the aggregate category count.

III. PROPOSED METHOD

The proposed GCN-centric framework for diagnosing bearing faults is structured around three pivotal components, detailed as follows: (1) Periodogram Extraction, (2) Graph Formulation, (3) Implementation of the GCN.

A. PERIODOGRAM EXTRACTION

As illustrated in [23], various bearing fault manifestations – including defects in the outer ring, inner ring, and rolling elements – are discernible within the periodogram derived from condition monitoring signals. Consider a signal, $x(n)$, procured by a sensor where n spans $[0, N-1]$ and N signifies the total sampling points within the time-domain signal. The signal’s discrete Fourier transform can be expressed as:

$$Y(k) = \sum_{n=0}^{N-1} x[n] \omega^*[n-M] e^{-j2\pi k \Delta f n} \quad (4)$$

where Δf symbolizes the frequency interval, $Y(k)$ denotes the output at frequency $k\Delta f$ for $0 < k < K$, the “*” indicates conjugation, and ω represents a window function, tailored based on the original signal’s attributes and the requisite balance between frequency and time resolution [19]. In this study, the periodogram is extracted utilizing the Hanning window. However, a detailed discourse on window selection lies beyond the purview of this paper.

Given the discrete Fourier transform of the initially captured signal, the periodogram, represented as F_k , can be computed as:

$$F_k = \frac{1}{T} |Y(k)|^2 \quad (5)$$

where F_k stands for the periodogram’s output at the frequency $k\Delta f$ with $0 < k < K$, and T indicates the duration of the window function (Fig. 2).

B. GRAPH FORMULATION

The graph model, characterized by its unique assembly of nodes and edges, provides a distinct representation of datasets through interconnected points and lines. This specific framework endows the graph model with two salient attributes:

- 1) It offers a holistic representation of the entire periodogram.
- 2) It elucidates the interrelations between frequency sampling points, facilitating this by crafting weighted edges through the integration of specific edges.

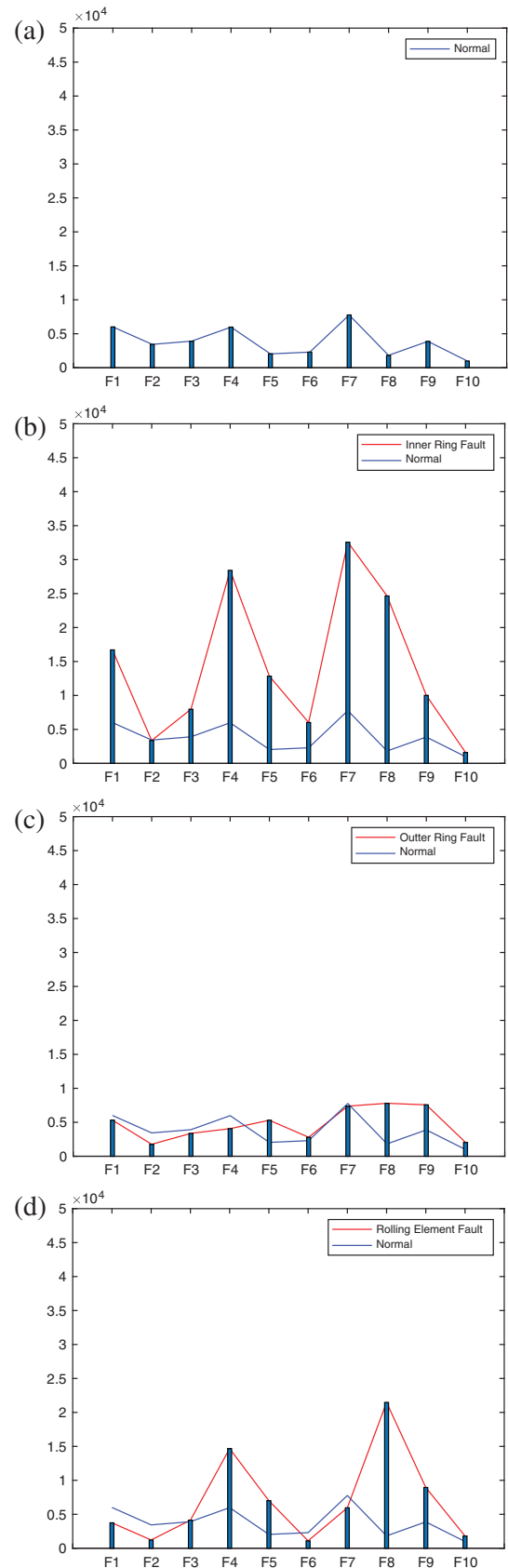


Fig. 2. A visual comparison of periodogram shifts across various bearing conditions: (a) normal, (b) inner-ring defect contrasted against the normal state, (c) outer-ring defect juxtaposed with the normal state, and (d) rolling element defect in comparison to its normal counterpart.

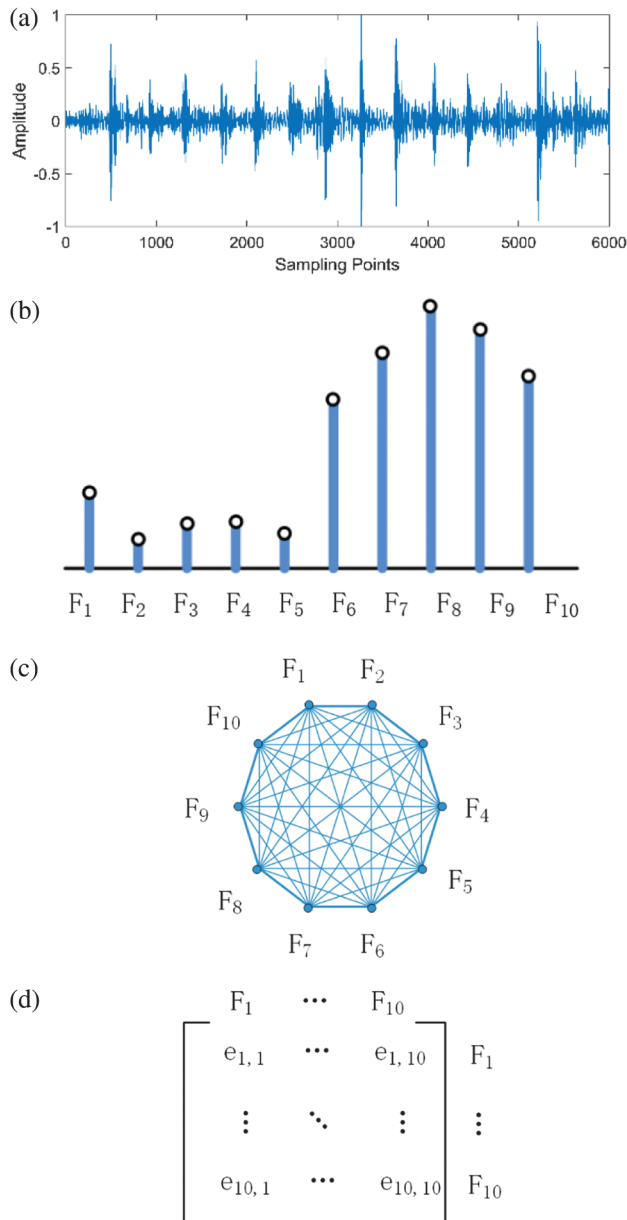


Fig. 3. The transformation of a vibration signal into a graph model: (a) original vibration signal; (b) derived periodogram; (c) constructed graph; and (d) the corresponding adjacency matrix.

To construct a representative structure for a given periodogram (Fig. 3), one can follow this systematic four-step procedure:

- Treat each frequency sampling point as an individual node within the graph model;
- Establish a weighted edge, denoted as L_{ij} , between every pair of sampling points, F_i and F_j ;
- Assign a specific weight, represented as e_{ij} , to each of these weighted edges;
- Illustrate the resulting graph using an adjacency matrix A , i.e., $A = \{e_{ij}\}$.

Within the graph's architecture, the weighted edges serve as indicators of the interconnectedness and correlation among nodes. Crucially, the pivotal aspect of this modeling hinges on the apt selection of weights for these edges. In the context of diagnosing bearing faults in rotating machinery,

this research introduces a specific weighting criterion as outlined:

$$e_{ij} = \text{Dis}\{F_i, F_j\} \quad (6)$$

where $\text{Dis}(\dots)$ represents the Euclidean distance.

These weights uniquely gauge the disparities between the frequency sampling points, with e_{ij} encapsulating the periodogram's frequency data.

With this, the graph representation of vibration signals associated with bearing faults is effectively finalized.

B. IMPLEMENTATION OF GCN

In this study, we introduce an algorithm rooted in the GCN for pinpointing bearing faults. This technique leverages graph data, derived from vibration signals, and employs a novel classification method to detect the nature of bearing faults.

The GCN approach we put forward can be primarily segmented into two stages: feature extraction and subsequent classification. During the feature extraction stage, a dual-layer graph convolution structure is employed to extract pertinent graph features, which entails conducting graph convolutions on vibration signal-derived graph data twice consecutively. In the classification stage, these discerned graph features are channeled into a softmax layer tasked with the classification of bearing fault signals. The comprehensive architecture of the proposed methodology is illustrated in Fig. 4.

The associated loss function is characterized by the cross-entropy discrepancy between the predicted softmax output's probability distribution and the desired class's probability distribution [24]. The mathematical representation of the loss function is:

$$H(p, q) = - \sum_x p(x) \log q(x) \quad (7)$$

where $p(x)$ delineates the target distribution, while $q(x)$ indicates the estimated distribution.

IV. EXPERIMENTS AND RESULTS

A. BEARING FAULT PLATFORM

In this study, we have developed an experimental platform tailored for gathering data on bearing faults, as visualized in Fig. 5. This platform primarily comprises a motor, a B&K type 4397 accelerometer, an advanced data acquisition system (utilizing the NI controller PXIe-8135 coupled with the NI acquisition board PXIe-6358), and an array of ten N205-type bearings. These test bearings are segmented into ten categories based on distinct fault conditions: a normal bearing; bearings showcasing inner-ring defects of 0.22 mm, 0.44 mm, and 0.66 mm; those with outer-ring aberrations of the aforementioned measurements; and those presenting rolling element irregularities of the same dimensions (further details provided in Fig. 6, Table I).

B. EXPERIMENTAL METHOD AND DATA COLLECTION

To evaluate the efficacy of the introduced approach, vibration signals from the ten distinct bearing sets are captured using an accelerometer. The motor operates at a speed of

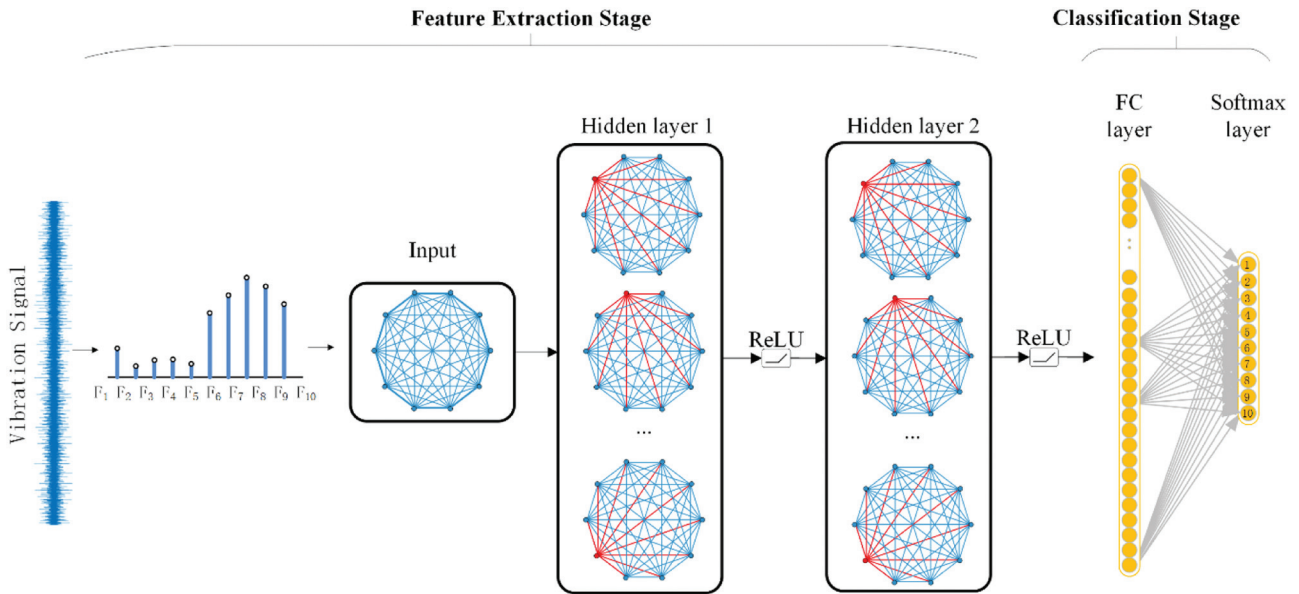


Fig. 4. The proposed GCN algorithm.

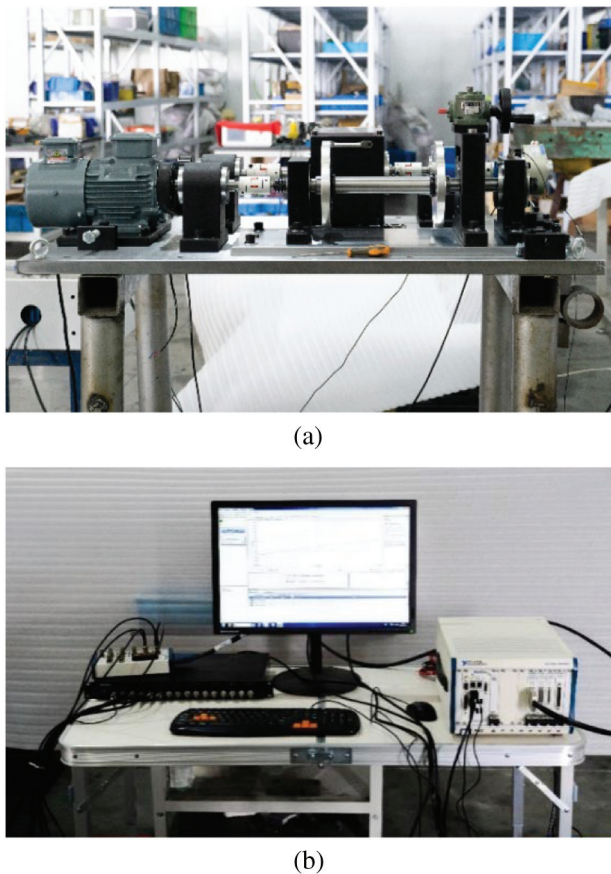


Fig. 5. Experimental setup for bearing fault data acquisition: (a) testing apparatus, (b) data acquisition ensemble.

1,490 rpm. With a sampling rate set at 48 kHz, each gathered signal spans a total of 1,920,000 data points.

Figure 7 illustrates the signal waveforms acquired from the ten bearing sets.

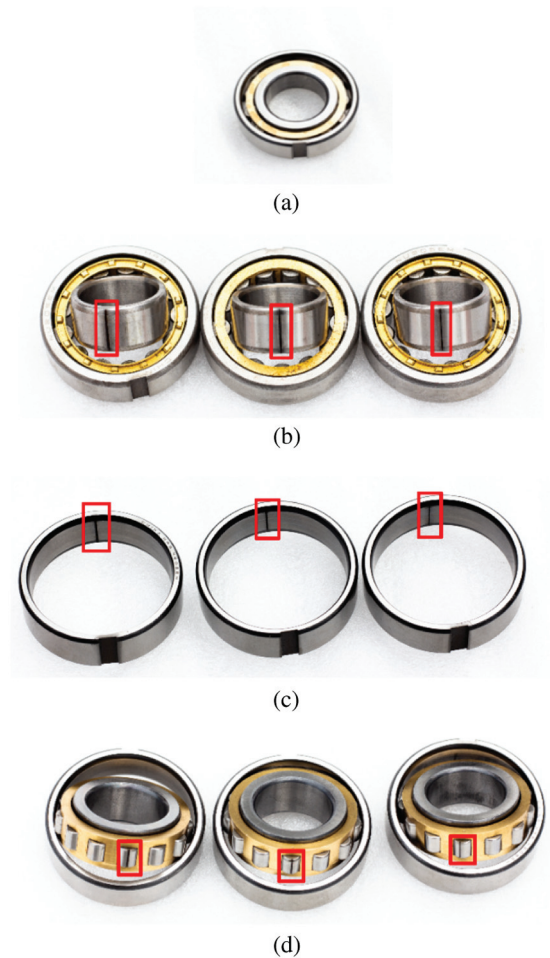


Fig. 6. Array of test bearings, categorized as (a) a flawless bearing, (b) those with inner-ring faults at 0.22 mm, 0.44 mm, and 0.66 mm, (c) those affected by outer-ring anomalies of 0.22 mm, 0.44 mm, and 0.66 mm, and (d) those revealing rolling element deformities of 0.22 mm, 0.44 mm, and 0.66 mm.

Table I. Bearing specifications employed in the experimental trials

Bearing type	Pitch diameter	Roller diameter	Roller number
N205	38.5 (mm)	6.5 (mm)	13

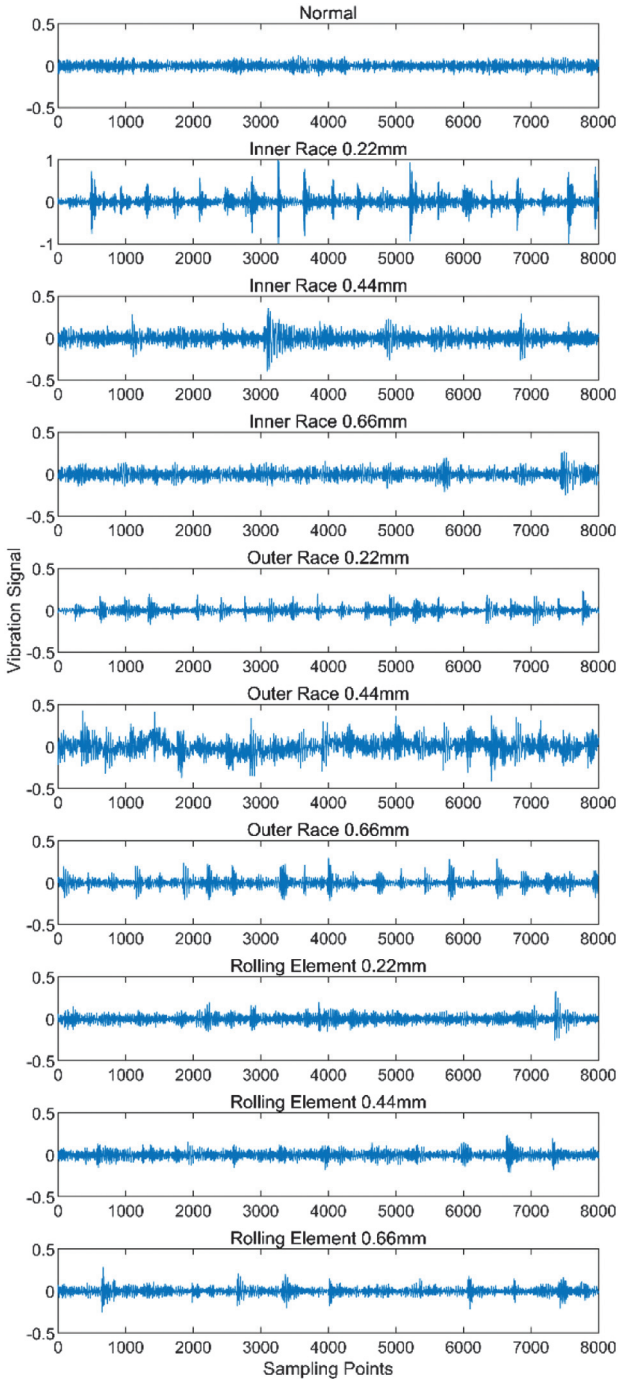


Fig. 7. Waveforms from the ten distinct bearing sets.

Subsequently, a dataset is constructed from these vibration signals. From each bearing group, 200 samples are secured, with every sample encompassing 8,192 vibration signal data points, as displayed in Fig. 8. These vibration signals, gathered from the ten bearing groups,

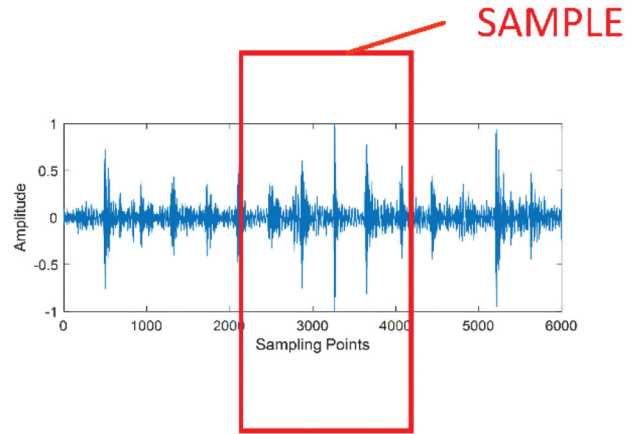


Fig. 8. Depiction of vibration data sampling from bearings.

Table II. Dataset details of the bearing faults

Bearing types	Label category
normal bearing	1
Inner-ring fault 0.22 mm	2
Inner-ring fault 0.44 mm	3
Inner-ring fault 0.66 mm	4
Outer-ring fault 0.22 mm	5
Outer-ring fault 0.44 mm	6
Outer-ring fault 0.66 mm	7
Rolling body fault 0.22 mm	8
Rolling body fault 0.44 mm	9
Rolling body fault 0.66 mm	10

are then categorized from 1 through 10. A comprehensive dataset is then assembled, integrating all these samples, detailed in Table II.

C. DIAGNOSTIC PRECISION OF THE PROPOSED METHOD

This section delves into the diagnostic precision of the introduced method across varying radial loads. We employ the original dataset from Table II, considering three distinct radial loads: 0 N, 50 N, and 100 N.

We further explore the correlation between the method’s precision and the iteration count. From this point forward, “accuracy” pertains to the proportion of samples that the classifier aptly categorizes relative to the complete sample count in a specific test dataset. This metric provides direct insight into the algorithm’s classificatory efficacy. After each iteration, a unique accuracy value emerges, resulting in 100 distinct values post 100 iterations. Figure 9(a)–(c) delineates the accuracy trajectory of our method across varied loads.

Figure 9(a)–(c) demonstrates that as the iteration count ascends, the accuracy curves consistently rise. This suggests that across all load scenarios, an increased number of iterations consistently enhances the diagnostic precision of the proposed method.

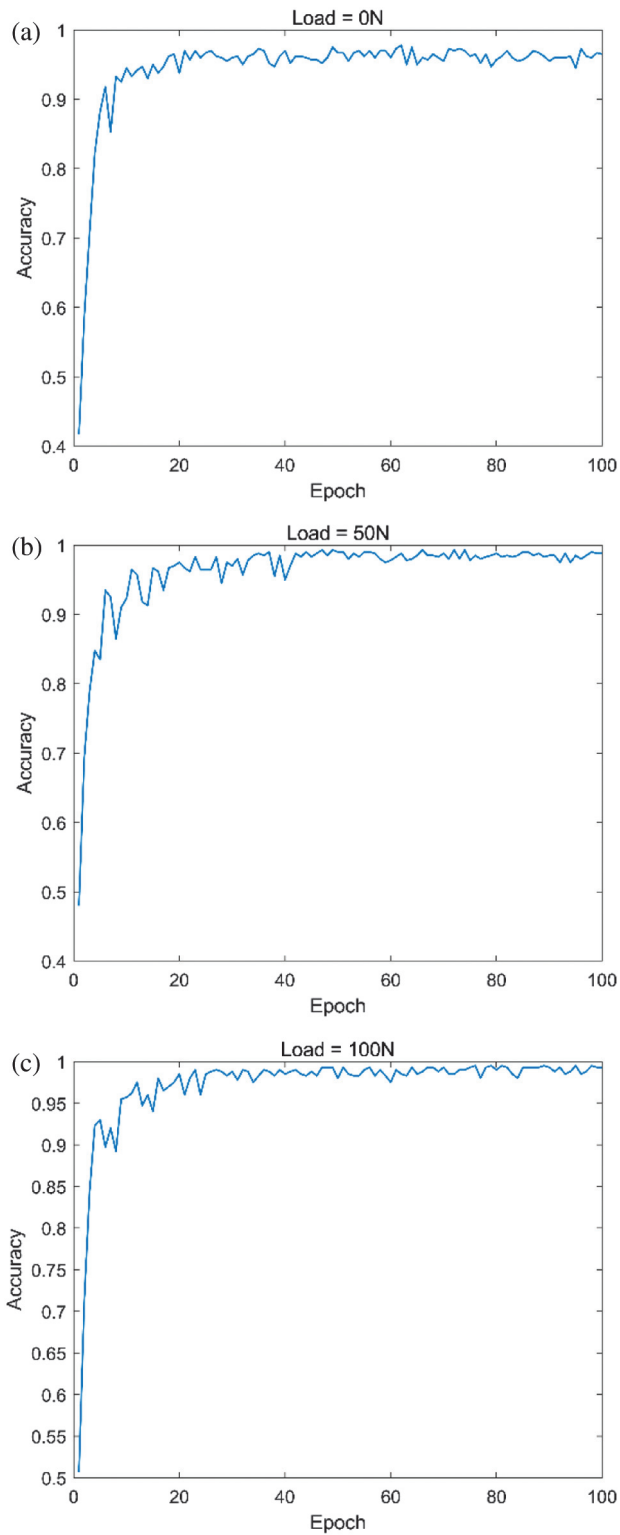


Fig. 9. Accuracy curves across three radial loads: (a) Load = 0 N, (b) Load = 50 N, and (c) Load = 100 N.

D. PERFORMANCE OF THE PROPOSED METHOD IN VARIED NOISE CONDITIONS

To align our testing closer with real-world situations, we evaluate our proposed method on signals across a range of SNRs. These are generated by introducing varying degrees of white Gaussian noise to the baseline dataset.

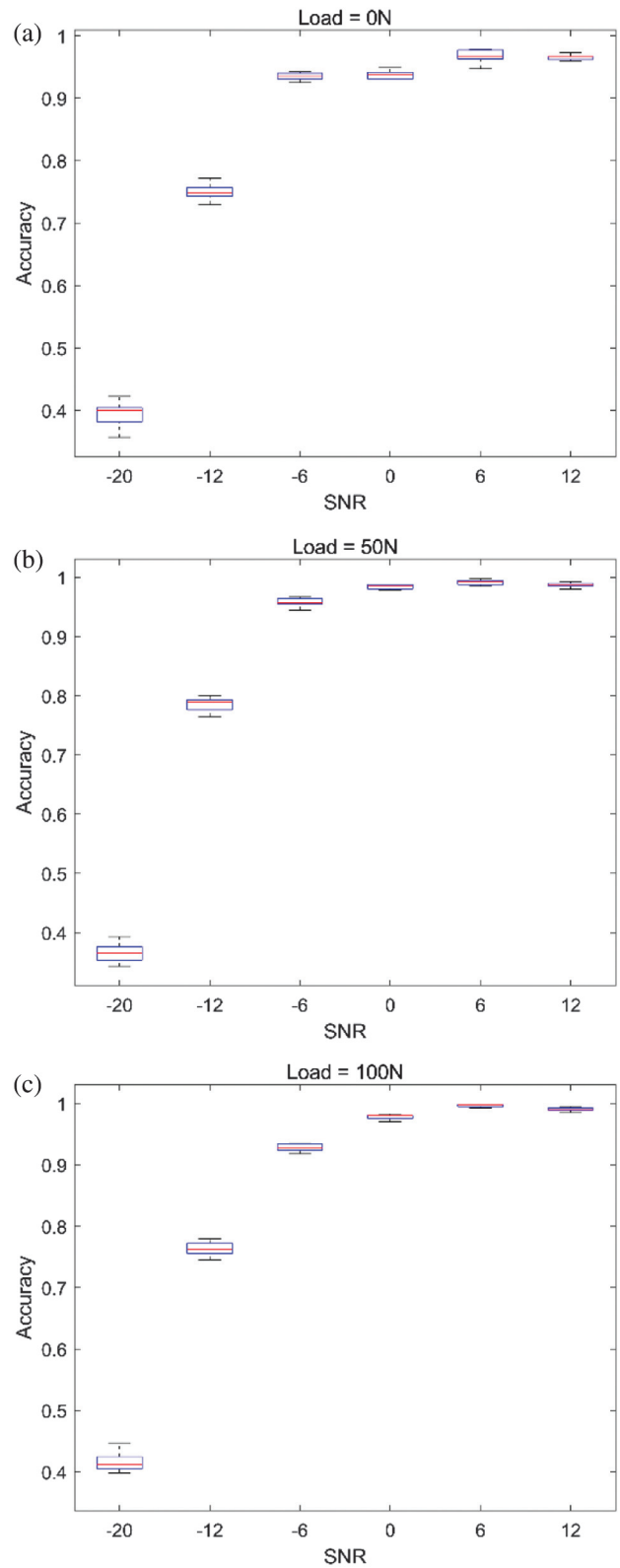


Fig. 10. Diagnostic accuracies across varying SNRs: (a) Load = 0 N, (b) Load = 50 N, (c) Load = 100 N.

The SNR definition is based on the formulation presented in reference [24]:

$$SNR_{dB} = 10 \log_{10} \left(\frac{P_{signal}}{P_{noise}} \right) \quad (8)$$

where P_{signal} and P_{noise} are the power of the signal and noise, respectively.

In this study, the introduced method is assessed under six distinct SNRs: SNR = -20 dB, SNR = -12 dB, SNR = -6 dB, SNR = 0 dB, SNR = 6 dB, and SNR = 12 dB. We aim to shed light on the diagnostic accuracy of the method within noisy conditions. To conduct this evaluation, the foundational dataset from Table II is subjected to three varying loads, each being superimposed with noise to emulate the six aforementioned SNRs. The algorithm's accuracy rates are computed across these SNRs, and the collective findings are illustrated in Fig. 10.

Observing Fig. 10(a)–(c), it becomes evident that under each of the three radial loads, the diagnostic accuracy of the GCN algorithm improves as the SNR rises. A plausible reason is that at higher SNRs, the amplitude energy of frequency sampling points in periodograms remains prominent, not overshadowed by noise. Consequently, the relationships among these frequency sampling points are delineated with greater precision.

E. COMPARISON WITH ESTABLISHED ALGORITHMS

While the efficacy of the proposed method for fault diagnosis has been validated earlier, we aim to further contextualize its proficiency in bearing fault diagnosis by

juxtaposing its accuracy against established algorithms in this realm. Particularly, we benchmark our method against renowned diagnostic algorithms including Graph-KNN [19], GCN Benchmark [21], WDCNN [13], FFT-BP [8], and FFT-SAE [25], all of which leverage vibration signals.

Taking a specific scenario where the dataset is characterized by “Load = 100N” and “SNR = 0 dB” as input parameters, our proposed method demonstrates an impressive accuracy rate of 97.82% post 100 iterations. In comparison:

The Graph-KNN algorithm, after converting vibration signals to graph data and subsequently feeding it into the KNN classifier, achieves an accuracy of 97.65% within the same iteration count.

The GCN Benchmark algorithm, after converting vibration signal to graph data by representing splitted time-domain signal segments as graph node features, and subsequently feeding it into the GCN Benchmark algorithm, achieves an accuracy of 92.77% within the same iteration count.

Using unprocessed vibration signals under identical load and SNR conditions, the WDCNN algorithm, upon channeling this data into its network, posts an accuracy score of 93.82% post 100 iterations.

The FFT-SAE algorithm, upon applying an FFT transformation to time-domain signals garnered from the

Table III. The diagnostic accuracy of the proposed method versus other algorithms at “Load = 0N”

Algorithm	SNR (dB)					
	-20	-12	-6	0	6	12
Proposed method	39.39% ± 0.0483%	74.87% ± 0.0128%	93.53% ± 0.0031%	93.71% ± 0.0042%	96.84% ± 0.0093%	96.55% ± 0.0014%
Graph-KNN	38.95% ± 0.0261%	67.40% ± 0.0341%	87.45% ± 0.0412%	92.75% ± 0.0017%	92.85% ± 0.0015%	93.85% ± 0.0013%
GCN benchmark	33.41% ± 0.0061%	66.34% ± 0.0473%	86.10% ± 0.0429%	93.34% ± 0.0093%	96.23% ± 0.0108%	93.53% ± 0.0070%
WDCNN	62.52% ± 0.0024%	63.82% ± 0.0015%	75.87% ± 0.0013%	86.38% ± 0.0012%	92.82% ± 0.0012%	94.34% ± 0.0011%
FFT-SAE	33.35% ± 0.0050%	47.19% ± 0.0065%	69.38% ± 0.0026%	88.43% ± 0.1454%	90.92% ± 0.3578%	94.40% ± 0.0011%
FFT-BP	49.27% ± 0.0016%	63.56% ± 0.0013%	75.29% ± 0.0012%	87.40% ± 0.0011%	92.64% ± 0.0011%	93.67% ± 0.0010

Table IV. The diagnostic accuracy of the proposed method versus other algorithms at “Load = 50N”

Algorithm	SNR (dB)					
	-20	-12	-6	0	6	12
Proposed method	36.55% ± 0.0216%	78.55% ± 0.0144%	95.84% ± 0.0045%	98.44% ± 0.0013%	99.22% ± 0.0019%	98.70% ± 0.0014%
Graph-KNN	38.80% ± 0.0327%	70.80% ± 0.0245%	92.40% ± 0.0089%	97.40% ± 0.0024%	98.45% ± 0.0031%	98.30% ± 0.0015%
GCN benchmark	38.82% ± 0.0061%	67.48% ± 0.0473%	81.19% ± 0.0429%	90.47% ± 0.0093%	96.70% ± 0.0108%	94.64% ± 0.0070%
WDCNN	75.43% ± 1.3604%	82.69% ± 0.0003%	80.85% ± 0.0019%	96.24% ± 0.0009%	97.70% ± 0.0011%	98.26% ± 0.0012%
FFT-SAE	41.28% ± 0.0095%	62.80% ± 0.0085%	80.36% ± 0.0044%	90.14% ± 0.0014%	95.87% ± 0.0011%	98.51% ± 0.0012%
FFT-BP	51.86% ± 0.0009%	77.19% ± 0.0004%	88.99% ± 0.0012%	93.26% ± 0.0016%	94.06% ± 0.0012%	94.48% ± 0.0010%

Table V. The diagnostic accuracy of the proposed method versus other algorithms at “Load = 100N”

Algorithm	SNR (dB)					
	-20	-12	-6	0	6	12
Proposed method	41.28% ± 0.0415%	76.32% ± 0.0121%	92.80% ± 0.0031%	97.82% ± 0.0016%	99.67% ± 0.0003%	99.06% ± 0.0010%
Graph-KNN	38.45% ± 0.0522%	70.65% ± 0.0236%	92.30% ± 0.0219%	97.65% ± 0.0157%	97.95% ± 0.0069%	97.95% ± 0.0141%
GCN benchmark	41.50% ± 0.0276%	66.68% ± 0.0170%	83.97% ± 0.0414%	92.77% ± 0.0324%	98.48% ± 0.0073%	97.82% ± 0.0282%
WDCNN	64.30% ± 0.0514%	68.21% ± 0.0024%	81.46% ± 0.0032%	93.82% ± 0.0014%	98.85% ± 0.0010%	98.38% ± 0.0011%
FFT-SAE	47.70% ± 0.0152%	54.31% ± 0.8879%	86.72% ± 0.0007%	90.10% ± 0.2201%	91.26% ± 0.0031%	98.67% ± 0.0023%
FFT-BP	52.28% ± 0.0013%	73.11% ± 0.0013%	87.52% ± 0.0022%	91.99% ± 0.0011%	93.92% ± 0.0018%	94.35% ± 0.0021%

accelerometer (under similar load and SNR), manages an accuracy of 90.10% after its 100th iteration once the FFT results are processed through the SAE network.

Lastly, the FFT-BP algorithm, when processing the frequency-domain signals acquired from the accelerometer under the same conditions, records an accuracy of 91.99% after 100 iterations.

These algorithms are also assessed across the remaining SNRs and loads, with all findings compiled in Tables III–V. It is noteworthy that the diagnostic performances of these algorithms exhibit disparities when sifting through the bearing fault signal dataset. Across all six SNRs, especially at relatively elevated SNR values, our proposed method, heralded as a novel diagnostic approach, not only outperforms the Graph-KNN and GCN Benchmark algorithm but also demonstrates superior accuracy rates against other counterparts like WDCNN, FFT-SAE, and FFT-BP that harness vibration signals.

V. CONCLUSION

Maintaining rotating machinery necessitates precise bearing fault diagnosis. While established deep learning methods excel in handling Euclidean data forms, including audio, image, and video, they falter when encountering non-Euclidean datasets, such as graphs. This study introduces an approach for bearing fault diagnosis: the GCN algorithm. This innovative technique classifies bearing faults by interpreting graphs derived from their vibration signals. Comprehensive experimental assessments shed light on its diagnostic precision across various loads and SNRs. Additionally, a comparative analysis positions the GCN algorithm vis-à-vis established algorithms like Graph-KNN, GCN Benchmark, WDCNN, FFT-SAE, and FFT-BP. Empirical results accentuate the superior diagnostic efficacy of our proposed method compared to the mainstream algorithms enumerated.

By ingeniously converting vibration signals into graph formulations and subsequently employing the GCN algorithm for classification, this research makes a significant contribution in refining bearing fault diagnostic accuracy. It is our aspiration that this avant-garde approach will pave the way for future innovations in the domain of intelligent fault diagnosis.

CONFLICT OF INTEREST STATEMENT

The authors declare no conflicts of interest.

REFERENCES

- [1] Y. Lei, J. Lin, and Z. He, “A review on empirical mode decomposition in fault diagnosis of rotating machinery,” *Mech. Syst. Signal. Process.*, vol. 35, pp. 108–126, 2013.
- [2] Z. Gao, C. Cecati, and S. X. Ding, “A survey of fault diagnosis and fault-tolerant techniques—part I: fault diagnosis with model-based and signal-based approaches,” *IEEE Trans. Ind. Electron.*, vol. 62, pp. 3537–3767, 2015.
- [3] V. K. Rai and A.R. Mohanty, “Bearing fault diagnosis using FFT of intrinsic mode functions in Hilbert–Huang transform,” *Mech. Syst. Signal. Process.*, vol. 21, pp. 2607–2615, 2007.
- [4] X. Lou and K. A. Loparo, “Bearing fault diagnosis based on wavelet transform and fuzzy inference,” *Mech. Syst. Signal. Process.*, vol. 18, pp. 1077–1095, 2004.
- [5] Y. Yu, D. J. Yu, and J. S. Cheng, “A roller bearing fault diagnosis method based on EMD energy entropy and ANN,” *J. Sound Vib.*, vol. 294, pp. 269–277, 2006.
- [6] B. Samanta and K. R. Al-Balushi, “Artificial neural network based fault diagnostics of rolling element bearings using time-domain features,” *Mech. Syst. Signal. Process.*, vol. 17, pp. 317–328, 2003.
- [7] P. Konar and P. Chattopadhyay, “Bearing fault detection of induction motor using wavelet and Support Vector Machines (SVMs),” *Appl. Soft. Comput.*, vol. 11, pp. 4203–4211, 2011.
- [8] B. Li, M. Y. Chow, Y. Tipsuwan, and J. C. Hung, “Neural-network-based motor rolling bearing fault diagnosis,” *IEEE Trans. Ind. Electron.*, vol. 47, pp. 1060–1069, 2000.
- [9] V. Muralidharan and V. Sugumaran, “A comparative study of Naive Bayes classifier and Bayes net classifier for fault diagnosis of monoblock centrifugal pump using wavelet analysis,” *Appl. Soft. Comput.*, vol. 12, pp. 2023–2039, 2012.
- [10] D. H. Pandya, S. H. Upadhyay, and S. P. Harsha, “Fault diagnosis of rolling element bearing with intrinsic mode function of acoustic emission data using APF-KNN,” *Expert Syst. Appl.*, vol. 40, pp. 4137–4145, 2013.
- [11] Z. Q. Chen, L. Chuan, and S. René-Vinicio, “Gearbox fault identification and classification with convolutional neural networks,” *Shock Vib.*, vol. 2, pp. 1–10, 2015.

- [12] O. Janssens et al., "Convolutional neural network based fault detection for rotating machinery," *J. Sound Vib.*, vol. 377, pp. 331–345, 2016.
- [13] W. Zhang, G. Peng, C. Li, Y. Chen, and Z. Zhang, "A new deep learning model for fault diagnosis with good anti-noise and domain adaptation ability on raw vibration signals," *Sensors*, vol. 17, p. 425, 2017.
- [14] B. Joan, Z. Wojciech, S. Arthur, and L. Yann, "Spectral networks and locally connected networks on graphs," 2013. arXiv preprint arXiv:1312.6203.
- [15] Z. M. Chen, X. S. Wei, P. Wang, and Y. W. Guo, "Multi-label image recognition with graph convolutional networks," in *Proc. IEEE Conf. Comput. Vis. Pattern Recogn.*, IEEE, Long Beach, California, USA, 2019, pp. 5177–5186.
- [16] H. Martin, D. Bucher, E. Suel, P. X. Zhao, P. C. Fernando, and R. Martin, "Graph convolutional neural networks for human activity purpose imputation," in *NIPS Spatiotemp. Workshp. 32nd Annu. Conf. Neural Inf. Process. Syst.*, NIPS Foundation, Montreal, Canada, 3–8 Dec. 2018, pp. 1–6.
- [17] G. Lu, J. Liu, and P. Yan, "Graph-based structural change detection for rotating machinery monitoring," *Mech. Syst. Signal Process.*, vol. 99, pp. 73–82, 2018.
- [18] T. Wang, G. Lu, and P. Yan, "A novel statistical time-frequency analysis for rotating machine condition monitoring," *IEEE Trans. Ind. Electron.*, vol. 67, pp. 531–541, 2020.
- [19] T. Wang, G. Lu, and P. Yan, "Fault diagnosis of rolling bearings based on undirected weighted graph," in *2019 Prognost. Syst. Health Manag. Conf.*, IEEE, Paris, France, 2–5 May 2019, pp. 30–34.
- [20] D. Zhang et al., "Intelligent acoustic-based fault diagnosis of roller bearings using a deep graph convolutional network," *Measurement*, vol. 156, p. 107585, 2020.
- [21] T. Li et al., "The emerging graph neural networks for intelligent fault diagnostics and prognostics: a guideline and a benchmark study," *Mech. Syst. Signal Process.*, vol. 168, p. 108653, 2022.
- [22] T. Ahmad, H. Mao, L. Lin, and G. Z. Tang, "Action recognition using attention-joints graph convolutional neural networks," *IEEE Access*, vol. 8, pp. 305–313, 2019.
- [23] L. Ciabattoni, F. Ferracuti, and A. Freddi, "Statistical spectral analysis for fault diagnosis of rotating machines," *IEEE Trans. Ind. Electron.*, vol. 65, pp. 4301–4310, 2017.
- [24] W. Zhang, C. Li, G. Peng, Y. Chen, and Z. Zhang, "A deep convolutional neural network with new training methods for bearing fault diagnosis under noisy environment and different working load," *Mech. Syst. Signal Process.*, vol. 100, pp. 439–453, 2018.
- [25] N. K. Verma, V. K. Gupta, M. Sharma, and R. K. Sevakula, "Intelligent condition based monitoring of rotating machines using sparse auto-encoders," in *Prognost. Health Manag.*, IEEE, Gaithersburg, MD, USA, 24–27 June 2013, pp. 1–7.